Tephrostratigraphy of proximal pyroclastic sequences at Mount Melbourne (northern Victoria Land, Antarctica): insights into the volcanic activity since the last glacial period.

P. Del Carlo[1], A. Di Roberto[1*], G. Di Vincenzo[2], G. Re[1], P.G. Albert[3], M. Nazzari[4], V.C. Smith[5], A. Cannata[6,7].

(1) Istituto Nazionale di Geofisica e Vulcanologia, Sezione di Pisa, via C. Battisti 53, 56125 Pisa, Italy

(2) Istituto di Geoscienze e Georisorse, Consiglio Nazionale delle Ricerche, (IGG-CNR), Via G. Moruzzi 1, 56124, Pisa, Italy

(3) Department of Geography, Swansea University, Singleton Park, Swansea, SA2 8PP, UK

(4) Istituto Nazionale di Geofisica e Vulcanologia, Sezione di Roma1, via di Vigna Murata 605, 00143, Roma, Italy

(5) Research Laboratory for Archaeology and the History of Art, School of Archaeology, University of Oxford, 1 South Parks Road, OX1 3TG, UK

(6) Dipartimento di Scienze Biologiche, Geologiche e Ambientali, Università di Catania, Corso Italia 57, 95125 Catania, Italy

(7) Istituto Nazionale di Geofisica e Vulcanologia, Osservatorio Etneo, Piazza Roma 2, 95125 Catania, Italy

*Corresponding author Alessio Di Roberto: alessio.diroberto@ingv.it

Keywords: Antarctica, Mount Melbourne, Explosive eruptions, Tephra, Glass geochemistry, ^{40}Ar-^{39}Ar dating

Abstract

We report on the characterization of a thick sequence of pyroclastic deposits exposed on the summit area and flanks of Mount Melbourne volcano, in northern Victoria Land,

Antarctica related to eruptions during the Late Glacial period. We provide a complete characterization of tephra deposits including mineralogy, single shard major- and trace-element glass compositions, and an ^{40}Ar-^{39}Ar age of feldspar crystals extracted from the deposit. The pyroclastic deposits are trachybasaltic to trachytic in composition and are interpreted to have resulted from four Strombolian/Vulcanian to sub-Plinian/Plinian eruptions. The younger and more intense sub-Plinian/Plinian eruption (our *eruption 2*) yielded an ^{40}Ar-^{39}Ar age of 13.5±4.3 ka (±2σ). The study of Mount Melbourne proximal deposits provides significant new data for the reconstruction of the volcano eruptive history and a better assessment of the volcanic risk connected to a possible future eruption.

We also explore geochemical correlations between Mount Melbourne proximal deposits and distal tephra layers recognized in ice cores and blue ice fields of East Antarctica. A good geochemical match exists between the composition of products from the trachytic sub-Plinian/Plinian *eruption 2* and some tephra layers from Talos Dome and shards in Siple Dome which is also compatible in age (c. 9.3 ka) with our ^{40}Ar-^{39}Ar age determination. Our new insights into the volcanic history of Mount Melbourne and the new high-quality electron microprobe and trace element composition data on its proximal products will help improve future correlations and synchronization of tephra archives in the region.

1. Introduction

Recent years have seen significant advances in our knowledge and understanding of Antarctic volcanism owing to the extensive research carried out during the seasonal presence of scientists and technicians on the continent. Geological surveys, and the installation and significant improvements to the ground-based monitoring networks at some of the active volcanoes are providing new data on the eruptive history of Antarctic volcanoes and their current status (Gambino et al., 2021; Geyer et al., 2021; Sims et al., 2021). In particular, the study of tephra (volcanic ash) layers produced by explosive eruptions of Antarctic volcanoes have provided relevant information about

source volcanoes and volcanic systems including the age of the eruptions, and the style and intensity of the volcanic activity (Del Carlo et al., 2015; Di Roberto et al., 2019; 2020; 2021a; Iverson et al., 2014; Lee and Lee, 2017; Lee et al., 2019; Narcisi et al., 2010; Narcisi and Petite, 2021 and references therein). In Antarctica, as in many other geographical contexts, tephra deposits are proving invaluable in paleoenvironmental and paleoclimate studies since they represented a powerful chrono-stratigraphical tool that can be used to date sedimentary archives, enable their correlation over significant distances, and link and synchronize different types of records (outcrops, marine sediments and ice cores; Di Roberto et al., 2021b).

In addition, the presence of permanent scientific bases in the vicinity of some of the Antarctic volcanoes (for example the Argentine and Spanish bases on Deception Island) and the rapidly growing tourism in the Antarctic region make it crucial to increase our knowledge of the eruptive history of these volcanoes, in order to define the potential hazards associated with future eruptions (Geyer et al., 2021). Mount Melbourne is one of the largest active volcanoes of Antarctica and the last eruption is thought to have occurred around 1892 CE (Geyer, 2021 and references therein). The Mario Zucchelli Station (Italian), Jang Bogo (Korea), Gondwana (Germany) bases and the new China station are located between 65 and 30 km from the summit of Mount Melbourne and are within the range of significant ash fallout in the case of an intense explosive eruption. In the second half of the 1980s, the Italian National Antarctic Research Program (PNRA) began numerous activities in northern Victoria Land, some of which were focused on investigating and monitoring Mount Melbourne volcano. In particular, a global positioning system (GPS), tilt and seismic networks were installed on the volcano summit and flanks, and a volcanological observatory was set up in 1988 (Bonaccorso et al., 1997). From 2016, new seismological, geochemical and volcanological research was carried out on Mount Melbourne in the framework of the ICE-VOLC Project. A review of the volcanological investigations and monitoring results achieved over the last 30 years for Mount Melbourne has been recently published by Gambino et al. (2021). In particular, these authors report that the volcano

shows signs of activity including the magmatic signature of geochemical fluids from active fumaroles, seismicity comprising both long-period events and tremor and ground deformation with evidence of slow inflation/deflation around the summit area. Further signs of relatively recent activity of Mount Melbourne include tephra exposures in the summit and flanks of the volcano (see Giordano et al., 2012 and references therein), which are thick and suggest that intense explosive eruptions occurred in the recent past. Mount Melbourne should be considered capable of producing large eruptions (VEI > 3) with high eruptive plumes, with the potential for transcontinental ash dispersal that could result in significant consequences to global aviation safety (Geyer et al., 2017). Consequently, it is critical to correctly assess the nature, dynamics, intensity, and recurrence interval of Mount Melbourne eruptions to evaluate the future potential volcanic hazard.

With this aim, a complete characterization of proximal deposits from high explosive eruptions of Mount Melbourne is of great importance. In this paper, we provide a volcanological reconstruction of activity that deposited the uppermost pyroclastic sequence of Mount Melbourne. We present geological data from field observations of the pyroclastic deposits exposed in the summit area and on the flank of the volcano, which were made during the XXXII Italian Antarctic Expedition (2016-2017) in the framework of the ICE-VOLC project (PNRA). We also sampled the units and provide the tephra characterization including mineralogy, major- and trace-element glass compositions, and ^{40}Ar-^{39}Ar data obtained on feldspar crystals extracted from a trachytic pumice deposit. Based on these data, we make inferences on the last cycle of eruptions from Mount Melbourne.

These new data are also useful for tephrochronological studies and in particular, for the precise identification of Mount Melbourne derived tephra layers. These tephra layers can now be used to assess reliable proximal-distal correlations and for the dating, correlation and synchronization of paleoclimate archives in the region.

2. Geological background

Northern Victoria Land is part of the McMurdo Volcanic Group, one of the largest areas of Cenozoic volcanic rocks in Antarctica. The northern Victoria Land hosts a very long record of rift-related igneous activity including plutonic rocks and cogenetic dyke swarms spanning from about 50 to 20 Ma. The volcanism in northern Victoria Land started in the middle Miocene (c. 15 Ma) with activity largely concentrated between the Late Miocene (<10 Ma) and the present (Smellie and Rocchi, 2021). The origin of the entire igneous suite was long debated but presently the most accepted model sees no role for a mantle plume (Rocchi and Smellie, 2021). According to this model, the growth of the largest volcanic edifices along the Ross Sea coast since the middle Miocene was governed by lithospheric necking. Conversely smaller central volcanoes and scoria cones located inland would result from the establishment of magma chambers in the thicker crust (Rocchi and Smellie, 2021). Volcanoes of the northern Victoria Land include quite large multiple coalesced shield volcanoes, relatively small stratovolcanoes, and tiny monogenetic volcanic centres with scoria cones that belong to two main volcanic provinces, the Hallett and Melbourne volcanic provinces (Smellie and Rocchi, 2021). In the Melbourne volcanic province, Mount Melbourne and Mount Rittmann volcanoes have been active in recent times as a large number of Late Pleistocene to Holocene tephra layers found in the glacial and marine archives have been correlated to these sources (Del Carlo et al. 2015; Di Roberto et al. 2019; Dunbar et al. 2003; Narcisi et al. 2010). Mount Melbourne is located between Wood Bay and Terra Nova Bay and is now quiescent (Figs. 1 and 2). The volcano has a basal diameter of c. 21-24 km and a maximum elevation of 2732 m. The edifice is largely covered by snow and ice, except for the summit region and sparse rock exposures on the east side that extend down to c. 1800 m in elevation. The volcano shows a gentle conical shape, with undissected flanks, apart from a small scar located on the eastern side that is possibly linked to a landslide event (Giordano et al., 2012), and has a well-formed ice-filled crater c. 700 m in diameter that has also been interpreted as a summit caldera (Armienti et al., 1991).

A comprehensive synthesis of Mount Melbourne volcanic evolution is presented in Wörner and Viereck (1990) and Giordano et al. (2012), which is based on stratigraphic and geochemical data and ^{40}Ar-^{39}Ar geochronology. The eruptive activity in the area appears to have started with the formation of several monogenetic scoria cones and lava flows over a wide area across the Transantarctic Mountains during the Lower Pleistocene (Random Hills Period), which were mainly fed by alkali basaltic to hawaiitic magmas. Afterwards, the volcanic activity became concentrated in the area of the present-day Mount Melbourne stratovolcano, where deposits of several monogenetic vents show the transition from subglacial/subaqueous to subaerial activity during the Middle Pleistocene (Shield Nunatak Period). The early activity of the Mount Melbourne stratovolcano is characterized by a trachytic ignimbrite that is dated at 123.6±6.0 ka (Giordano et al. 2012) and indicates the formation of a crustal magma system (Mount Melbourne Period). Following the ignimbrite, a succession of alkali basaltic, hawaiitic, and subordinate benmoreitic lavas and scoria cones, dated at 90.7±19.0 ka, were emplaced. The most recent deposit exposed at the top of Mount Melbourne is mainly trachytic to rarely rhyolitic pumice fall deposits, probably produced by a Plinian eruption (Giordano et al., 2012).

Presently, there is an extensive fumarolic and geothermal activity in the crater and on the flanks of the volcano. The fumaroles have also produced several ice towers and a complex network of ice caves near the summit area (Gambino et al., 2021; Lyon and Giggenbach, 1974; Lyon, 1986; Worner and Viereck, 1990)

The age of the last eruption from Mount Melbourne is still uncertain and there have been no direct observations. Tephra layers have been found in glacier ice at several places on the flanks of Mount Melbourne, suggesting that explosive activity may have occurred in recent times. Lyon (1986) carried out the stable isotope analysis of two snow profiles, at ca. 2000 m on the flanks of Mount Melbourne and the Campbell Glacier, and estimated a snow accumulation rate of 0.5 and 2.2 m/a, respectively. Using this accumulation rate, Lyon (1986) derived an age between 1862 and 1922 CE for the

uppermost ash layer that was found in an ice cliff on the western slope of Mount Melbourne.

Tephra layers have been also mapped on the eastern flanks of Mount Melbourne by Lee and Lee (2017) and Lee et al. (2019). These are grey, m-thick composed of pumice and crystals and yellowish-grey trachytic, pumice lapilli up to 20 cm-in diameter, embedded in ice. Based on the correlation between these proximal deposits and ash layers found in the Talos Dome ice core, Lee et al. (2020a, b) suggest there have been three Holocene eruptions from Mount Melbourne. The major element glass compositions of Talos Dome tephra layer TD85, dated at 670 ± 7 a BP (Narcisi et al., 2012; Severi et al., 2012), is thought to represent a Mount Melbourne eruption with the same age (the second one in stratigraphic order found by Lee and Lee (2017) and Lee et al. (2019) on Mount Melbourne proximal sites).

3. Materials and methods

In the austral summer of 2016-17, during the XXXII Italian Antarctic Expedition, we measured, described, and sampled the uppermost pyroclastic sequence exposed in the summit area and along the northern-western flank of Mount Melbourne volcano (Figs. 1, 3 and 4).

The samples were mounted in epoxy resin, sectioned and polished for the textural and geochemical analyses at the Istituto Nazionale di Geofisica e Vulcanologia, Sezione di Pisa (INGV-Pisa). A scanning electron microscope (SEM) was used to describe textures, and an Oxford Si(Li) energy-dispersive X-ray detector (EDS) was also used to determine mineral phase compositions. Major and minor element glass compositions of samples were determined using a JEOL 8600 wavelength-dispersive electron microprobe equipped with four spectrometers at the Research Laboratory for Archaeology and the History of Art, University of Oxford (operating conditions: 15 kV accelerating voltage, 6 nA beam current and a beam diameter of either 10 or 5 μm depending on the glass surface areas). The JEOL 8600 electron microprobe was calibrated with a suite of appropriate mineral standards; peak count times were 30 s for

all elements except Mn (40s), Na (12s), Cl (50s), P (60s). The PAP absorption correction method was used for quantification. Reference glasses from the Max Planck Institute (MPI-DING suite; Jochum et al., 2005) bracketing the possible chemistries were also analysed. These included felsic [ATHO-G (rhyolite)], through intermediate [StHs6/80-G (andesite)] to mafic [GOR132-G (komatiite)] glasses. All glass data have been normalised to 100% for comparative purposes. Uncertainties are typically < ± 0.8% Relative Standard Deviation (RSD) for Si and ~ ± 5% for most other major elements, except for the low abundance elements for instance Ti (~± 7 %) and Mn (~± 30%). Additional analyses were conducted at the HPHT Laboratory INGV-Roma using a JEOL JXA 8200 electron microprobe equipped with five wavelength-dispersive spectrometers (operating conditions: 15 kV accelerating voltage, 8 nA beam current, 5 µm probe diameter, 10 and 5 s acquisition time for peak and background, respectively). For JEOL JXA 8200 EMPA the following standards were used: orthoclase (Si, Al, K and Na), apatite (F, P and Ca), forsterite (Mg), pyrite (Fe), rutile (Ti), tugtupite (Cl), and rhodonite (Mn). Sodium and potassium were analyzed first to prevent alkali migration effects. The precision of the microprobe was measured through the analysis of well-characterized synthetic oxide and mineral secondary standards. Based on counting statistics, analytical uncertainties relative to their reported concentrations indicate that for major elements precision was better than 5%. Analytical totals <93 wt.% were discarded. Error bars on plots represent reproducibility, calculated as 2SD (standard deviation) of replicate analyses of MPI-DING StHs6/80-G.

The full glass dataset and the standard data are reported in Supplementary Table 1. Trace element analysis of volcanic glass was performed using an Agilent 8900 triple quadrupole ICP-MS (ICP QQQ) coupled to a Resonetics 193 nm ArF excimer laser-ablation in the Department of Earth Sciences, Royal Holloway, University of London. Full analytical procedures used are reported in Tomlinson et al. (2010). Spot sizes 20 and 25 mm were used depending on the vesicularity, crystal content, and ultimately the size of available glass surfaces. The repetition rate was 5 Hz, with a count time of 40 s on the sample, and 40 s on the gas blank to allow the subtraction of the background

signal. Blocks of eight or nine glass shards and one MPI-DING reference glass were bracketed by the NIST612 glass calibration standard (GeoREM 11/2006). In addition, MPI-DING reference glasses were used to monitor analytical accuracy (Jochum et al., 2005). The internal standard applied was ^{29}Si (determined by the EPM analysis). LA-ICP-MS data reduction was performed in Microsoft Excel. Accuracies of LA-ICP-MS analyses of MPI-DING glass standards ATHO-G and StHs6/80-G were typically <5%. Full glass datasets and MPI-DING standard glass analyses are provided in Supplemental Material 1.

^{40}Ar-^{39}Ar analyses were completed on a feldspar separate (grain size 0.25-0.50 mm), which was extracted from pumice lapilli through standard separation techniques, followed by handpicking under a stereomicroscope (sample MELS1-3). ^{40}Ar-^{39}Ar analyses were determined through the laser step-heating technique at IGG-CNR (Pisa, Italy). The separate was leached in an ultrasonic bath at room temperature for a few minutes in diluted HF (7%) and was then wrapped in aluminium foil and irradiated in two distinct batches along with either the flux monitor Fish Canyon Tuff sanidine (irradiation PAV-80 lasting 5 hours) or the Alder Creek sanidine (irradiation PAV-82, lasting 2 hours). Irradiation for both batches was completed in the core of the TRIGA reactor at the University of Pavia (Italy). Argon isotope compositions for irradiation PAV-80 were acquired by a MAP215–50 single-collector noble gas mass spectrometer, fitted with a secondary electron multiplier. Gas purification (13 min, including ~3 min of lasering) was achieved by two SAES AP10 getters held at 400 °C, one SAES C-50 getter held at room temperature and a liquid nitrogen cold trap. Blanks were analyzed every three to four analyses. A polynomial function was fit to blanks analyzed during the day of acquisition, and unknown analyses were corrected based on the time of measurement. Blanks are listed in Supplementary Table 2. Argon isotope compositions for irradiation PAV-82 were acquired by an ARGUS VI (Thermo Fisher Scientific) multi-collector noble gas mass spectrometer. Ar isotopes from 40 to 37 were acquired using Faraday detectors, equipped with 10^{12} Ω resistors for ^{40}Ar and ^{38}Ar and 10^{13} Ω resistors for ^{39}Ar and ^{37}Ar. Faraday detectors were cross calibrated for the slight offset

using air shots. ^{36}Ar intensities were acquired by a Compact Discrete Dynode (CDD) detector. The CDD is calibrated daily for its yield by measuring four to six air pipettes prior to the first analysis. Gas purification (4 min, including ~3 min of lasering) was achieved using three SAES NP10 getters (one water-cooled, held at ~400 C and two at room temperature). Blanks were monitored every two runs and were subtracted from succeeding sample results (Supplementary Material 2). More details about mass spectrometer calibration and analysis can be found in Di Vincenzo et al. (2021). Mass discrimination for both measurements acquired through the MAP215-15 and the ARGUS VI mass spectrometers was determined before and after sample measurements based on automated analyses of air pipettes (Supplementary Table 2). About 50 mg of the feldspar separate from irradiation PAV-80 was spread onto the bottom of a 9-mm hole of a copper holder, loaded into a vacuum chamber comprising a laser port consisting of a ZnSe window fitted with a differentially pumped flange, and baked for 12 h at 150°C. Step-heating experiments were performed using a CO_2 laser beam (New Wave Research MIR10–30 CO_2 laser system) defocused to a ~2 mm spot size and slowly rastered over the sample. Steps were carried out at increasing laser power until complete melting. Six feldspar grains from irradiation PAV-82, which were selected among the largest and inclusion-free grains, were instead placed into a 3-mm diameter of a copper holder and baked and incrementally heated as above. Ar isotope concentrations are reported in Supplementary Table 2 and have been corrected for blank, mass discrimination, radioactive decay and line blanks. Uncertainties on step ages are 2σ analytical uncertainties, including in-run statistics and uncertainties in the discrimination factor, interference corrections and procedural blanks. Uncertainties on the total gas ages and error-weighted means also include the uncertainty on the fluence monitor (2σ internal errors). Ages were calculated relative to an FCs age of 28.201 (Kuiper et al., 2008), which is consistent with an ACs age of 1.1848 Ma (Niespolo et al., 2017), using decay constants recalculated by Min et al. (2001) and an atmospheric $^{40}Ar/^{36}Ar$ ratio of 298.56±0.31 (Lee et al., 2006).

4. Results

4.1 Deposit characteristics and stratigraphy

The summit portion of the Mount Melbourne volcano was surveyed during eleven helicopter flights and seven fieldwork campaigns. Unfortunately, most of the volcano is covered by snow and only a few summit exposures of the pyroclastic sequence thought to be associated with the last eruptions are accessible for observation and sampling. The uppermost pyroclastic succession was found in two small trenches dug on the volcano flank (sections S1 and S5; Figs. 3 and 4), and in three natural exposures hereafter named stratigraphic sections S2, S3 and S4 (Figs. 3 and 4). Some other outcrops near the summit were visited and described but the exposure was limited and insufficient to help constrain the event stratigraphy and aid interpretation of the pyroclastic deposit sequence.

Section S1 was dug on the northern summit area (-74.34953 S, 164.69148 E) at an altitude of 2605 m (Fig. 1). The pyroclastic succession is 40-60 cm-thick and consists of massive, moderately sorted, clast-supported, and inversely graded pumice deposits with clasts ranging from fine lapilli to bombs (Fig. 3a). The deposit is made of angular to sub-angular highly vesicular, light-grey pumice lapilli and blocks with minor fine-grained ash matrix (samples MELS1-2-3-4). Larger pumice bombs, up to 30 cm in diameter, are concentrated in the topmost part of the sequence and often have broken in situ and show a jigsaw-fit texture. Lithic fragments are rare and include dark grey lava fragments and oxidized clasts as large as 6 cm (ML 4).

The sequence overlies a dark grey to black, ash and scoriaceous lapilli bed (sample MELS1-1) that is >20 cm-thick (the base is not exposed), and it is capped by a polymictic breccia mainly consisting of sparse pumice blocks and lapilli, dark to reddish scoria fragments, and dense, variably altered lava clasts that are described in detail in Giordano et al. (2012) (Fig. 3a). The dark scoriaceous bombs are up to 1 m in diameter, occasionally have fluidal shapes and are scattered on the surface of the deposit (sample MELS1-5; Fig. 4a).

Section S2 is located on the northeast slope of Mount Melbourne (-74.34933 S, 164.71756 E), at 2278 m of altitude (Fig. 1). The sequence is 210 cm thick and comprises several stacked beds of clast-supported, ash-matrix-free, coarse pumiceous lapilli, which alternate with alignments and lenses of pumice bombs (samples MELS2-1-2-3-3bis-4) that are often bread-crusted and up to 45 cm in diameter (Fig. 3b). In the uppermost part of the section, the pumice lapilli deposit inversely grades into a c. 50 cm-thick bed made of decimeter-sized, dark brown to reddish pumice bombs (Fig. 3b). Lithic fragments are present but scarce along the entire sequence and are mainly represented by red-oxidized clasts and minor dark lava fragments that are <7 cm.

Section S3 comprises lenses and a massive deposit of centimeter-sized pumiceous lapilli that is <1 m-thick (sample MELS3-1). These deposits are observed in depressions and sheltered places on the top of a parasitic cone (1815 m of altitude) and on the northern flank of Mount Melbourne (-74.3253 S, 164.6286 E; Fig. 4b and c).

Section S4 is exposed inside the northern wall of Mount Melbourne crater (-74.3506 S, 164.6994 E) at an elevation of 2526 m (Figs. 1 and 3c). It was described from a distance as it is located in a quasi-vertical exposure. At this site, the pyroclastic sequence is the thickest observed and is >15 m-thick (the base is not exposed). It is a massive pumice lapilli unit with scattered bombs up to c. 30 cm in diameter (sample MELS4-1). Like in section S2, the uppermost c. 1 m of the sequence comprises a dark brown to reddish bed made of pumice bombs and blocks up to c. 1 m in diameter. This unit is partially welded and it is capped by a lithic breccia comprising blocks to lapilli-sized, black to orange-reddish moderately vesicular scoria and dense lava fragments (Fig. 3c).

A black poorly sorted deposit, partially covered by snow, crops out on the surface in the southern inner side of the crater. It is made of scoriaceous bombs (often breadcrusted) and lapilli (sample MELS5-1) and overlies the massive pumice deposit (-74.3578 S, 164.6994 E; Figs. 1 and 4d).

4.2 Clast textures and mineral compositions

Analysed samples from different pyroclastic units display distinctive textural, petrographic and geochemical features.

Sample MELS1-1 (Fig. 5a), which represents the lowermost stratigraphic unit, consists of porphyritic scoria with <500 μm euhedral phenocrysts and microphenocrysts of labradorite plagioclase (An_{50-58}), olivine (<110 μm; Fo_{71}), augite clinopyroxene (up to 80 μm; Wo_{42}-En_{41}-Fs_{17}), and Fe-Ti spinel (up to 60 μm), set in a dark glassy groundmass with abundant skeletal microlites of the same mineral phases. Some plagioclase phenocrysts display a reverse zoning pattern with sub-rounded anhedral cores of andesine composition (An_{38}).

Samples MELS1-2-3-4 (Section S1), MELS2-1-2-3-4 (Section S2), MELS3-1 (Section S3), and MELS4-1 (Section S4) represent the main pumice lapilli unit and show consistent textural and petrographic features across the different stratigraphic sections. These pumices (Fig. 5b) are highly vesicular, with spherical, tubular, and coalesced bubbles. In the majority of samples, the groundmass is glassy and clear, but the MELS2-4 and MELS4-1 samples have a light brown groundmass. In all pumice samples, the groundmass contains scarce euhedral to subhedral phenocrysts of feldspar up to 2 mm with anorthoclase to oligoclase compositions (An_{16-27}) (Supplementary Table 3). Some of the larger crystals occasionally show a sieve texture and most contain melt inclusions (Fig. 5b). Samples also contain phenocrysts of aegirine-augite clinopyroxene (up to 500 μm; Wo_{45}-En_{20}-Fs_{35}), olivine (Fo_{15}; up to 750 μm), Fe-Ti spinel (up to 200 μm) and apatite microphenocrysts (50 μm). Glomerophyres of plagioclase, clinopyroxenes, apatite and Fe-Ti oxides often occur.

Sample MELS1-5 (Section S1; Fig. 5c) is porphyritic scoria, containing sparse phenocrysts of oligoclase plagioclase (up to 750 μm; An_{18-22}), anhedral to subhedral Fe-rich olivine (up to 950 μm; Fo_{15}), Fe-augite clinopyroxene (up to 220 μm; Wo_{44}-En_{21}-Fs_{35}), Fe-Ti oxide (up to 170 μm), and minor apatite (up to 60 μm) in a brown cryptocrystalline groundmass with abundant acicular microlites of anorthoclase (Or_{28}) and minor glass.

Sample MELS5-1 (Section S1; Fig. 5d) is porphyritic scoria with abundant crystals of plagioclase (up to 580 µm; An_{22-37}) that plot across the boundary between andesine and oligoclase in the ternary classification diagram of feldspars, olivine (up to 290 µm; Fo_{41}), augite clinopyroxene (up to 200 µm; Wo_{42}-En_{35}-Fs_{23}) with oscillating zonation, Fe-Ti oxide and apatite (up to 150 µm). Phenocrysts and microphenocrysts are dispersed in a light brown, glassy groundmass containing scarce microlites of plagioclase, clinopyroxene and Fe-Ti spinel.

4.3 Major and trace element glass geochemistry

The complete geochemical dataset including major, minor, and trace element glass compositions is reported as Supplementary Material 1. Major oxides have been recalculated to 100% on an anhydrous basis, and uncertainties are reported as 2 standard deviations (s.d.).

Sample MELS1-1 glass composition plots mainly in the trachybasalt field of the Total Alkali versus Silica (TAS) diagram (LeBas et al., 1986; Fig. 6a, b) with some analyses extending into the basaltic trachyandesite field (Fig. 6). The average SiO_2 content is 50.05 ± 0.69 wt.% and an alkali (Na_2O+K_2O) content between 5 and 7 wt.% with a low alkali ratio (K_2O/Na_2O = 0.60 ± 0.07). The average contents of the other major oxides are 8.95 ± 0.50 wt.% CaO, 12.44 ± 1.09 wt.% FeO_{tot}, and 14.02 ± 0.35 wt.% Al_2O_3 (Fig. 6 and Supplementary Material 1).

Samples belonging to the main pumice lapilli deposit (MELS1-2-3-4 and MELS2-1-2-3-4) exhibit extremely homogeneous major element glass compositions that plot in a very narrow cluster within the trachyte field of the TAS diagram (LeBas et al., 1986; Fig 6a, b). Average SiO_2 contents is 65.13 ± 0.31 wt.%, total alkali (Na_2O+K_2O) content is 10.69 ± 0.28 wt.%, whilst the glasses display a low alkali ratio (K_2O/Na_2O = 0.86 ± 0.03). The average contents of other major oxides are 1.90 ± 0.20 wt.% CaO, 5.34 ± 0.15 wt.% FeO_{tot}, and 15.79 ± 0.28 wt.% Al_2O_3 (Fig. 6 and Supplementary Material 1).

Sample MELS1-5 plots in a loose cluster within the trachyte field of the TAS diagram with a mean composition similar to those of samples from the main pumice deposits. The MELS1-5 glasses contain average major element contents of 64.8 ± 0.33 wt.% SiO_2, 1.36 ± 0.37 wt.% CaO, 5.64 ± 0.36 wt.% FeOt, and 15.68 ± 0.45 wt. % Al_2O_3, which are very similar to those of the main pumice fall unit, however, these glasses have more variable total alkali contents that range between 10 and 13 wt.% (Fig. 6a, b and Supplementary Material 1).

Finally, sample MELS5-1 is a homogeneous and trachytic in composition with an average SiO_2 content of 61.5 ± 0.26 wt.% and Na_2O+K_2O = 10.30 ± 0.12 wt.% (Fig. 6a, b). Other major oxides are also homogeneous with 2.77 ± 0.09 wt.% CaO, 8.14 ± 0.19 wt.% FeO_{tot}, and 15.18 ± 0.24 wt.% Al_2O_3 (Fig. 6 and Supplementary Material 1). Consistent with the major element data, the samples of the main pyroclastic unit (MELS1-2, MELS1-3 and MELS2-1-2-3) show homogeneous trace element volcanic glass compositions. Multivariate trace elements compositional diagrams in Figure 7 reveal homogeneous content of incompatible trace elements including Th (21 ± 0.5 ppm), Y (55 ± 4 ppm), Zr (693 ± 40 ppm), Nb (165 ± 6 ppm), and the Rare Earth Elements (REE). Ratios of High Field Strength Elements (HFSE) to Th remain constant within the glasses analysed (e.g., Nb/Th = 8.05 ± 0.19; Ta/Th = 0.43; and Zr/Th = 33.7 ± 0.89). Sample averages normalized to the primitive mantle (McDonough and Sun, 1995) reveal that the volcanic glasses display enrichment in the Light REE relative to the Heavy REE where La/Yb = 19 ± 0.84, while Sr (150 ± 12 ppm) shows a pronounced negative anomaly (Sr/Pr_N = 7.13 ± 0.30; Fig. 8) along with Ba to a lesser extent, both diagnostic of feldspar fractionation (Fig. 8).

Similar compositions also characterize sample MEL5-1 which is the highly porphyritic scoria on top of the main pumice fallout sequence. This sample shows very homogeneous trace element volcanic glass compositions with Th (22.5 ± 0.6 ppm), Y (63±1.8 ppm), Zr (740±21 ppm), Nb (182±4 ppm), and the REE. Ratios of HFSE to Th remain constant within the glasses analysed (e.g. Nb/Th = 8.12 ± 0.11; Ta/Th = 0.46; and Zr/Th = 33.05 ± 0.58) and are similar to the underlying pumice unit.

Conversely, sample MEL1-1, the trachybasaltic lapilli layer at the base of the main pumice sequence, shows significantly lower levels of incompatible trace elements enrichment. For instance Th (7.6 ± 1 ppm), Y (36 ± 4 ppm), Zr (312 ± 38 ppm), Nb (82 ± 12 ppm), and the REE all display lower concentrations than the overlying trachytes. This sample does show a positive anomaly in Sr (582 ± 31 ppm) and no negative anomaly in Ba. (Fig. 8).

4.4 ^{40}Ar-^{39}Ar data

^{40}Ar-^{39}Ar analysis on a feldspar separate (sample MELS1-3) was first acquired with an old generation single-collector noble-gas mass spectrometer, which required a large aliquot of separated mineral (tens of milligrams) corresponding to several tens of grains. The step ages were also affected by very large analytical uncertainties, due to the generally low radiogenic Ar content (Supplementary Table 2) and to the analytical capabilities of the mass spectrometer. Step ages, although displaying enormous scatter (from 271 ka to negative values, Fig. 9 and Supplementary Material 2), overlap within analytical uncertainties and yield an apparent weighted mean age of 122 ± 33 ka, which is in agreement with the total gas age of 140 ± 56 ka. K/Ca ratios, derived from neutron-produced $^{39}Ar_K$ and $^{37}Ar_{Ca}$ isotopes, define an overall descending profile (Fig. 9), ranging from 1.2 to 0.45, with a total gas K/Ca ratio of 0.61 ± 0.06. Crystals from the same mineral separate were later analyzed by a new generation multi-collector noble gas spectrometer, which permitted analysis on a much smaller quantity of sample, in the order of a few milligrams. This allowed selection of the largest (<2 mm), euhedral and inclusion-free grains. The step-heating analysis yielded much more precise data, with an overall descending age profile (Fig. 9), with ages ranging at face value from 45 to 4 ka. Excluding the first two steps, the remaining step age define a concordant segment representing ~87% of the total $^{39}Ar_K$ released and yielding an apparent weighted mean age of 13.5 ± 4.3 ka, in fairly good agreement with the total gas age of 17.3 ± 6.4 ka. K/Ca ratios, derived from neutron-produced Ar isotopes, define a gently descending profile, from ~0.55 to ~0.39 (total gas K/Ca of 0.45 ± 0.05), significantly

458 lower than those from the step-heating experiment completed on the larger sample
459 aliquot.
460 In light of the petrographic observations and chemical data presented above on both
461 feldspar and glass from sample MELS1-3, more specifically the K/Ca measured in the
462 glass (mean 3.21±0.14, ±SD, Supplementary Table 3) in the feldspar (mean 0.49±0.11,
463 ±SD, Supplementary Table 3), and attesting to the presence of glass inclusions in the
464 mineral separate, we assign the contrasting results between the two analyzed aliquots
465 to contamination by excess Ar (parentless ^{40}Ar) hosted in melt inclusions. The younger
466 ages observed for the smaller aliquot may be explained by a much less contaminated
467 sample, due to a better selection of the grain investigated. Strictly speaking, the
468 13.5±4.3 ka age should be considered as a maximum estimate for the age for the fallout
469 pumice deposit.
470

471 **5. Discussion**

472 *5.1 Eruptive sequence and dynamics*

473 The pyroclastic sequence exposed on the summit part of Mount Melbourne starts with
474 the dark, trachybasaltic, scoriaceous lapilli and ash unit (Fig. 3a). The fine-grained,
475 massive and clast supported characteristics of the trachybasaltic scoriaceous lapilli and
476 texture of particles forming the deposit (sample MELS1-1) are consistent with a mildly
477 explosive Strombolian eruption (*eruption 1*) from a vent located in the summit area.
478 Trachybasaltic scoria deposits are directly in contact with the overlying pumice
479 trachytic lapilli sequence, and no trace of erosion is evident, nor altered volcaniclastic
480 material interposed between the two deposits. This suggests that both eruptions were
481 probably separated by a relatively short period of time (months/few years).
482 We interpret the thick pumice lapilli and bombs deposit and the lithic-rich breccia
483 (samples MELS1-2-3-4 and MELS2-1-2-3-4) as different parts of the same eruptive
484 event (*eruption 2;* Fig. 10). The pumice lapilli and bombs unit is interpreted as a fallout
485 deposit (as it comprised of multiple massive, clast-supported pumice beds of unabraded

angular to sub-angular fragments that often have an in situ jigsaw-fit texture) erupted during the acme of an intense highly explosive eruption. The multiple cycles of reverse grading that characterizes the unit potentially reflects variations in the plume height and the intensity of the eruption during the waxing and waning of a pulsating column or could be linked to changes in the wind direction (Wilson et al., 1980). The lithic-rich breccia on top of the sequence associated with partially welded m-sized pumice bombs and blocks could indicate that after the emplacement of the main lapilli unit, there was an erosion of the vent walls or crater collapse. Widening or collapsing of the vent with the consequent incorporation of a dense lithic fraction should have led to an increase in the eruptive plume density and finally to its collapse and the deposition of the coarse-grained, proximal lithic and pumice-rich breccia. Similar deposits corresponding to proximal lag breccias or a crater collapse breccia (see Walker 1985) are quite widespread in deposits associated with large caldera collapse (Druitt and Bacon, 1986; Bear et al., 2009). Armienti et al. (1991) proposed that the Mount Melbourne crater is a small caldera, but they did not provide supporting evidence. It is not possible to know if the studied pyroclastic sequence ended with the emplacement of the lithic breccia. However, our observations indicate no evidence of significant erosion, so we hypothesize that it was erupted during the final stages of activity. Also Vulcanian-style explosive eruptions can produce massive heterolithic breccias made of angular, accessory lithics of various nature with minor accidental juvenile fragments. Thus, a second hypothesis may be that the lithic-rich breccia on top of the sequence is the result of a discrete Vulcanian explosion that occurred after the cessation of the main eruptive sequence.

The summit deposits described by Wörner et al. (1989), Wörner and Viereck (1990), and Giordano et al. (2012) are similar to those studied here by us in our in section S4. They report that along the rim of the summit crater the ground is covered by an accumulation of dark grey juvenile lapilli, <70 cm-thick punctuated by scattered bombs up to 50 cm in diameter, plus abundant polymictic lithic blocks. The deposit is interpreted as a coarse-grained fallout possibly related to the last explosive eruption of

Mount Melbourne. In the crater wall, this deposit overlies, with a gradational transition, a >15 m-thick pumice lapilli fallout deposit. The limited number of exposures hampers the reconstruction of isopach, isomass and isopleth maps and hinders retrieval of the key physical parameters of the eruption, such as the erupted volume and mass, plume height, and mass discharge rate. Inferences on the eruption intensity can be made only on the basis of the thickness and architecture of the deposit in the proximal facies, which suggest a sub-Plinian to Plinian eruption. On the basis of ^{40}Ar-^{39}Ar data, the age of this eruption is ≤13.5±4.3 ka. In the northern sector of the summit area of Mount Melbourne, the top of trachytic pumice lapilli unit has scattered dark volcanic blocks and bombs that are up to c. 50 cm in diameter and trachytic in composition (sample MELS1-5; Figs. 4a and 10). This deposit potentially represents the products of a small-scale eruption possibly of Strombolian or Vulcanian style (*eruption 3*) that occurred just after the sub-Plinian/Plinian eruption (*eruption 2*). Alternatively, also considering that the geochemical composition of the two deposits is quite similar, the latter could represent a late phase of the previous *eruption 2*.

Finally, according to their characteristics, the scoria lapilli and bombs of trachytic composition, recovered in the southern sector of the caldera (Fig. 4d and 10; sample MELS5-1), can be interpreted as deriving from another eruption and could be linked to the formation of one of the scoria cones/fissures in the southern sector of the caldera (*eruption 4*). Considering the deposit characteristics (e.g. structure, thickness, and distribution) the eruption must have been energy significantly lower than that of *eruption 2*. This eruption occurred after the large sub-Plinian/Plinian eruption (*eruption 2*) that deposited the main sequence of trachytic pumiceous lapilli; conversely, we cannot constrain the chronological relationship with the deposits of *eruption 3* in the northern sector of the summit area of Mount Melbourne because exposures do not show them in direct stratigraphic contact.

The studied deposits have glass geochemical compositions ranging from trachybasalt to trachyte (Fig. 6a). Samples plot on a well-defined compositional trend typical of products of Mount Melbourne (Lee et al., 2019; Rocchi and Smellie, 2021). The less

544 evolved trachybasalt-basaltic trachyandesite compositions are observed in the
545 stratigraphically lowermost sample (MELS1-1), while the later samples are all evolved
546 and trachytic in composition (MELS2-1-2-3-4 and MELS1-5);
547 From a geochemical point of view, the studied sample show homogeneous major and
548 trace element glass compositions, both within and between deposits. Only the MELS1-
549 1 (trachybasalt-basaltic trachyandesite) and MELS1-5 (trachyte) samples have glass
550 compositions that display wide internal variation in the alkali contents, which could be
551 related to late stage crystallization of microlites that vary in abundance. No mineralogic
552 or geochemical evidence of significant magma mingling/mixing occurs (e.g. banded
553 clasts or mixing/mingling texture in mineral phases). Mineral phases are fairly
554 homogeneous in composition although some feldspar crystals show sieve textures,
555 which indicate they were not in continuous equilibrium in the magmatic system and
556 suggest the system was recharged or they were incorporated as antecrysts during
557 crystallization. In general, each eruption was fed by a relatively homogeneous melt.
558

559 *5.3 Proximal-distal correlation*

560 The trachytic pumices from MELS2-1-2-3-4 and MELS1-5 in the main pyroclastic unit
561 (*eruption 2*) are geochemically indistinguishable from the compositions of tephra
562 previously sampled on the eastern flanks of Mount Melbourne and in particular with
563 MMTep004, 005, 007, 008, and 020 of Lee and Lee (2017), and samples A1602, 1604
564 and 1605 of Lee et al. (2019). This suggests that the samples of Lee and Lee (2017)
565 and Lee et al. (2019) possibly derive from the same eruptions studied here.
566 To test the possible correlation between studied deposits and other proximal deposits
567 of Mount Melbourne with more distal tephra layers found in records of Antarctica we
568 compared the major- and trace-element (when available) compositions with those of
569 tephra layers found in ice cores, marine sediments, blue ice and continental outcrops
570 (Figs. 6 and 7). We dedicated special attention to tephra layers found in the Talos
571 Dome, Styx Glacier and GV7 ice cores, as well as Frontier Mountain and Brimstone
572 Peak blue-ice fields records since they are the closest sites to Mount Melbourne

573 volcano and thus the best candidates to host tephra and cryptotephra derived from the
574 studied eruptions. Talos Dome is located at c. 250 km from Mount Melbourne, Styx
575 Glacier c. 100 km and GV7 ice core site c. 350 km, whereas Frontier Mountain and
576 Brimstone Peak blue-ice fields are c. 210 and 190 km, respectively. Considering the
577 apparent age of ≤13.5±4.3 ka of the main sub-Plinian/Plinian eruption studied here, we
578 limited the research to the c. 18 ka to the recent.
579 A compositional similarity exists between the glass composition of trachy-basaltic
580 deposits representative of the older eruption studied here (*eruption 1*), Talos Dome
581 glass shards concentrations TD238a (237.31 m) and TD388-2b (387.76 m). The latter
582 have ages of 2684±47 a BP and 5277±49 a BP, respectively (Severi et al., 2012; Narcisi
583 et al., 2012), and are attributed to Mount Melbourne by Narcisi et al. (2012). A broad
584 compositional affinity also exists between the glass composition of the main trachytic
585 pumice deposit (*eruption 2*) and many tephras and cryptotephra layers found at
586 different depths in the ice core record of Talos Dome. These include TD85 (84.37 m),
587 TD210 (209.50 m), TD238b (237.31 m), TD388 (387.76 m), and TD662 (661.86 m),
588 that correspond to a wide age interval between 670±7 a BP and 11,364±132 a BP
589 (Severi et al., 2012). Among these layers, the greatest geochemical similarities occur
590 with the TD85 tephra layer (Fig. 6) which was dated at 670±7 yrs BP (or 1280±7 C.E.)
591 by Severi et al. (2012) and is attributed to Mount Melbourne by Narcisi et al. (2012).
592 Despite the geochemical similarities, the significant age difference with the TD85
593 tephra and the age determined for *eruption 2* (13.5±4.3 ka) makes their correlation
594 unlikely. A good compositional match also occurs between the deposits of *eruption 2*
595 (samples MELS1-2-3-4 and MELS2-1-2-3-4) and a shard population in sample
596 SDMA-9007, which represents a visible 1 mm thick tephra layer found at a depth of
597 539.012 m in the Siple Dome ice record. The latter is predominantly rhyolitic in
598 composition and dated at 9355±2 yrs BP (Kurbatov et al., 2006). In this case, however,
599 our age determination for *eruption* 2 (13.5±4.3 ka) is indistinguishable within 2σ error
600 limits. Unfortunately, there are no single shard laser ablation trace element data for this
601 tephra, and there are only data for selected samples in the 16.5 and 71 ka age interval

for Talos Dome (see Narcisi et al., 2012). Trace element glass compositions for the Last Glacial to Holocene age interval are required to make robustr correlations. No compositional similarity exists between trachytic sample MELS5-1 representative of the youngest eruption of Mount Melbourne studied (*eruption 4*) and any currently analyzed tephra and cryptotephra found in the Talos Dome ice core or other ice records around Mount Melbourne volcano. However, the closest ice records to Mount Melbourne only span a limited timeframe, with the Styx Glacier spanning the last c. 1800 yrs (Yang et al. 2018; Kim et al. 2020) and GV7 only spanning the last c. 1000 yrs (Nardin et al. 2021). The comparison between the proximal deposits of Mount Melbourne (Lee and Lee, 2017; Lee et al., 2019; this work), and tephra in the glacial record clearly shows that there is no correlation between the proximal pyroclastic deposits and the distal tephra in the glacial archives that were previously attributed to Mount Melbourne. For instance, in the glacial record of Talos Dome, most of tephra or cryptotephra identified in the last c. 15 ka (total of 23 layers) have been attributed to the Mount Melbourne volcano area (Narcisi et al., 2012), but there is only evidence for four explosive eruptions around the summit of the volcano (Lee et al. 2020a, b; this work). Of these eruptions, only one of the deposits (*eruption 2*) displays features that are typically associated with eruptions that produce far-travelled ash and could have potentially reached the Talos Dome site. The other three eruptions possibly had mild Strombolian dynamics or were discrete Vulcanian explosions with energy arguably less compatible with producing ash layers as far as 250 km from the source. Two hypotheses can explain this discrepancy: i) the record of proximal pyroclastic deposits is very fragmented due to erosion and/or glacial cover, and is not fully representative of the activity of Mount Melbourne. This seems questionable because eruptions capable of depositing ash layers at considerable distances from the source would emplace thick pyroclastic sequences in the proximal areas (even if other deposits could be present at deeper levels but unexposed). Alternatively, ii) many of the tephra and cryptotephra previously attributed to Mount Melbourne were sourced from different volcanoes, despite erupting trachytic compositions that are similar to those of Mount

Melbourne. This again highlights that high-quality electron microprobe and trace element compositions of representative samples for the proximal deposits and distal tephra layers are needed for reliable correlation and the synchronization of tephra archives. In particular, trace element compositions are invaluable for the reliable identification of volcanic sources, and specific eruption deposits, especially for sequential eruptions that have similar major element compositions and to identify temporal and spatial petrological and geochemical variations in pyroclastic rocks from Antarctica.

6 Conclusions

Stratigraphic, mineralogical and geochemical characterization of deposits exposed around Mount Melbourne has improved our understanding of the eruptive history of this volcano. We recognized four different deposits in well-defined stratigraphic positions that are characterized by different textures, mineralogies, and geochemical compositions. These deposits correspond to four explosive eruptions (*eruptions 1, 2, 3 and 4*), ranging from Strombolian/Vulcanian to sub-Plinian/Plinian, and with compositions from trachy-basaltic to trachytic perfectly matching with the composition of the Mount Melbourne products that were previously reported by Lee and Lee, (2017) and Lee et al. (2019).

On the basis of the ^{40}Ar-^{39}Ar laser data, the age of the largest of the recognized eruptions that deposited a very thick fallout of trachytic pumice is $\leq 13.5 \pm 4.3$ ka which is likely to be a maximum estimate. Another age-based determination from a less advanced analytical instrument suggests an older age and probably the result of considerable contamination by xenocrysts.

Based on the comparison between the glass compositions in the studied deposits and that in englacial tephra layers found in ice cores around Mount Melbourne we can conclude that Mount Melbourne is the likely source for many of the tephra and ash particles identified. Unfortunately, there are no clear correlations between proximal and distal deposits so the dates of the eruptions are uncertain. For example, the glass

compositions of several proximal tephra on Mount Melbourne are similar to tephra layers recovered in Talos Dome and Siple Dome ice cores records. In particular, a good geochemical match exists between the glass composition of the main trachytic pumice at Mount Melbourne with TD85 tephra layer in Talos Dome that is too young (670±7 yrs BP), and a geochemical population of the SDMA-9007 visible tephra layer found in Siple Dome ice record that is dated at 9355±2 yrs BP and falls in the age interval of *eruption* 2. To facilitate reliable correlations and synchronization of tephra archives, high-quality electron microprobe and trace element compositions of representative samples are required.

Mount Melbourne is an active volcano and a potential danger for the nearby scientific stations and aviation safety across Antarctica. The permanent settlement and seasonal presence of scientists, technicians, tourists and logistical personnel close to this active volcano have increased significantly in the last decades. Given that the last eruptions were explosive and associated with evolved magma compositions, sub-Plinian/Plinian explosive activity could potentially occur in the future. Moreover, the presence of ice enhances the risk of hydrovolcanic eruptions, which due to magma–water interaction could turn small volume eruptions into highly explosive ash-forming events (e.g. White and Houghton, 2006). The monitoring network that is set up around Mount Melbourne is thus essential to assess signs of unrest.

Acknowledgements

This workwas funded by the Projects: ICE-VOLC (multiparametrIC Experiment at Antarctica VOLCanoes: data from volcano and cryosphere-ocean-atmosphere dynamics, www.icevolc-project.com/data; PNRA 14_00011) and TRACERS (TephRochronology and mArker events for the CorrElation of natural archives in the Ross Sea, Antarctica; PNRA2016 - Linea A3/00055). We acknowledge PNRA, the Italian *Programma Nazionale di Ricerche in Antartide*, for funding the projects and ENEA for providing field logistics at Mario Zucchelli Station. We are grateful to the pilots J. Henery and B. McElhinney for helicopter surveys and the INGV-OE colleague

689 G. Larocca and Italian alpine guide D. De Podestà for their help in the fieldwork. Dr.
690 C. Manning is also acknowledgement for assistance with the LA-ICP-MS analysis.
691 This paper is sponsored by the SCAR Expert Group, AntVolc. We would like to
692 sincerely thank Prof. J.L. Smellie and another anonymous reviewer for detailed and
693 constructive comments and suggestions that improved this manuscript.
694

695 **References**

696 Adamson, R.G., Cavaney, R.J., 1967. Volcanic Debris-Layers near Mount Melbourne,
697 Northern Victoria Land, Antarctica. New Zeal. J. Geol. Geophys. 10, 418–421.
698 https://doi.org/10.1080/00288306.1967.10426745

699 Armienti, P., Civetta, L., Innocenti, F., Manetti, P., Tripodo, S., Villari, L., Vita, G.,
700 1991. New petrological and geochemical data on Mt. Melbourne Volcanic Field,
701 Northern Victoria Land, Antarctica. (II Italian Antarctic Expedition). Mem. Soc. Geol.
702 It., 46, 397-424

703 Armstrong, R.L., 1978. K-Ar dating: Late Cenozoic McMurdo Volcanic Group and
704 dry valley glacial history, Victoria Land, Antarctica. New Zeal. J. Geol. Geophys. 21,
705 685–698. https://doi.org/10.1080/00288306.1978.10425199

706 Bear, A.N., Cas, R.A.F., Giordano, G. 2009. The implications of spatter, pumice and
707 lithic clast rich proximal co-ignimbrite lag breccias on the dynamics of caldera forming
708 eruptions: The 151 ka Sutri eruption, Vico Volcano, Central Italy. J. Volcanol.
709 Geotherm. Res. 181(1-2), 1-24. https://doi.org/10.1016/j.jvolgeores.2008.11.032

710 Bonaccorso A, Gambino S., Falzone G., Privitera E., 1997. The volcanological
711 observatory of the Mt. Melbourne (Northern Victoria Land, Antarctica). In: "The
712 Antarctic Region: Geological evolution and processes", C.A. Ricci (Ed.), Terra
713 Antartica Publication, Siena, 1083-1086.

714 Del Carlo, P., Di Roberto, A., Di Vincenzo, G., Bertagnini, A., Landi, P., Pompilio,
715 M., Colizza, E., Giordano, G., 2015. Late Pleistocene-Holocene volcanic activity in

716 northern Victoria Land recorded in Ross Sea (Antarctica) marine sediments. Bull.
717 Volcanol. 77, 36. https://doi.org/10.1007/s00445-015-0924-0

718 Di Roberto, A., Colizza, E., Del Carlo, P., Petrelli, M., Finocchiaro, F., Kuhn, G., 2019.
719 First marine cryptotephra in Antarctica found in sediments of the western Ross Sea
720 correlates with englacial tephras and climate records. Sci. Rep. 9, 10628.
721 https://doi.org/10.1038/s41598-019-47188-3

722 Di Roberto, A., Albert, P.G., Colizza, E., Del Carlo, P., Di Vincenzo, G., Gallerani, A.,
723 Giglio, F., Kuhn, G., Macrì, P., Manning, C.J., Melis, R., Miserocchi, S., Scateni, B.,
724 Smith, V.C., Torricella, F., Winkler, A., 2020. Evidence for a large-magnitude
725 Holocene eruption of Mount Rittmann (Antarctica): A volcanological reconstruction
726 using the marine tephra record. Quat. Sci. Rev. 250, 106629.
727 https://doi.org/https://doi.org/10.1016/j.quascirev.2020.106629

728 Di Roberto, A., Scateni, B., Di Vincenzo, G., Petrelli, M., Fisauli, G., Barker, S.J., Del
729 Carlo, P., Colleoni, F., Kulhanek, D.K., McKay, R., De Santis, L., The IODP
730 Expedition 374 Scientific Party, 2021a. Tephrochronology and Provenance of an Early
731 Pleistocene (Calabrian) Tephra From IODP Expedition 374 Site U1524, Ross Sea
732 (Antarctica). Geochemistry, Geophys. Geosystems 22, e2021GC009739.
733 https://doi.org/https://doi.org/10.1029/2021GC009739

734 Di Roberto, A., Del Carlo, P., Pompilio, M., 2021b. Chapter 6.1 Marine record of
735 Antarctic volcanism from drill cores. Geol. Soc. London, Mem. 55, 631 LP – 647.
736 https://doi.org/10.1144/M55-2018-49

737 Di Vincenzo, G., Folco, L., Suttle, M.D., Brase, L., Harvey, R.P., 2021. Multi-collector
738 40Ar/39Ar dating of microtektites from Transantarctic Mountains (Antarctica): A
739 definitive link with the Australasian tektite/microtektite strewn field. Geochim.
740 Cosmochim. Acta 298, 112–130.
741 https://doi.org/https://doi.org/10.1016/j.gca.2021.01.046

742 Druitt, T.H., Bacon, C.R. 1986. Lithic breccia and ignimbrite erupted during the
743 collapse of Crater Lake Caldera, Oregon. J. Volcanol. Geotherm. Res. 29(1-4), 1-32.
744 https://doi.org/10.1016/0377-0273(86)90038-7

745 Gambino, S., Armienti, P., Cannata, A., Del Carlo, P., Giudice, G., Giuffrida, G.,
746 Liuzzo, M., Pompilio, M., 2021. Chapter 7.3 Mount Melbourne and Mount Rittmann.
747 Geol. Soc. London, Mem. 55, M55-2018–43. https://doi.org/10.1144/M55-2018-43

748 Geyer, A., Marti, A., Giralt, S., Folch, A., 2017. Potential ash impact from Antarctic
749 volcanoes: Insights from Deception Island's most recent eruption. Sci. Rep. 7, 16534.
750 https://doi.org/10.1038/s41598-017-16630-9

751 Geyer, A., 2021. Chapter 1.4 Antarctic volcanism: active volcanism overview. Geol.
752 Soc. London, Mem. 55, M55-2020–12. https://doi.org/10.1144/M55-2020-12

753 Geyer, A., Pedrazzi, D., Almendros, J., Berrocoso, M., López-Martínez, J., Maestro,
754 A., Carmona, E., Álvarez-Valero, A.M., de Gil, A., 2021. Chapter 7.1 Deception
755 Island. Geol. Soc. London, Mem. 55, M55-2018–56. https://doi.org/10.1144/M55-
756 2018-56

757 Giordano, G., Lucci, F., Phillips, D., Cozzupoli, D., Runci, V., 2012. Stratigraphy,
758 geochronology and evolution of the Mt. Melbourne volcanic field (North Victoria
759 Land, Antarctica). Bull. Volcanol. 74, 1985–2005. https://doi.org/10.1007/s00445-
760 012-0643-8

761 Harpel, C.J., Kyle, P.R., Dunbar, N.W., 2008. Englacial tephrostratigraphy of Erebus

762 volcano, Antarctica. J. Volcanol. Geoth. Res. 177, 549e568.
763 https://doi.org/10.1016/j.jvolgeores.2008.06.001.

764 Iverson, N.A., Kyle, P.R., Dunbar, N.W., McIntosh, W.C., Pearce, N.J.G., 2014.
765 Eruptive history and magmatic stability of Erebus volcano, Antarctica: Insights from

englacial tephra. Geochemistry, Geophys. Geosystems 15, 4180–4202. https://doi.org/https://doi.org/10.1002/2014GC005435

Jochum, K.P., Pfänder, J., Woodhead, J.D., Willbold, M., Stoll, B., Herwig, K., Amini, M., Abouchami, W., Hofmann, A.W., 2005. MPI-DING glasses: New geological reference materials for in situ Pb isotope analysis. Geochemistry, Geophys. Geosystems 6. https://doi.org/https://doi.org/10.1029/2005GC000995

Kim, D., Prior, D.J., Han, Y., Qi, C., Han, H., Ju, H.T., 2020. Microstructures and Fabric Transitions of Natural Ice from the Styx Glacier, Northern Victoria Land, Antarctica. Minerals 10, 892. https://doi.org/10.3390/min10100892

Kuiper, K.F., Deino, A., Hilgen, F.J., Krijgsman, W., Renne, P.R., Wijbrans, J.R., 2008. Synchronizing Rock Clocks of Earth History. Science, 320, 500–504. https://doi.org/10.1126/science.1154339

Kurbatov, A. V, Zielinski, G.A., Dunbar, N.W., Mayewski, P.A., Meyerson, E.A., Sneed, S.B., Taylor, K.C., 2006. A 12,000 year record of explosive volcanism in the Siple Dome Ice Core, West Antarctica. J. Geophys. Res., 111, D12307. https://doi.org/https://doi.org/10.1029/2005JD006072

LeBas, M.J.L., Maitre, R.W.L., Streckeisen, A., Zanettin, B., IUGS Subcommission on the Systematics of Igneous Rocks, 1986. A Chemical Classification of Volcanic Rocks Based on the Total Alkali-Silica Diagram. J. Petrol. 27, 745–750. https://doi.org/10.1093/petrology/27.3.745

Lee, J.-Y., Marti, K., Severinghaus, J.P., Kawamura, K., Yoo, H.-S., Lee, J.B., Kim, J.S., 2006. A redetermination of the isotopic abundances of atmospheric Ar. Geochim. Cosmochim. Acta 70, 4507–4512. https://doi.org/https://doi.org/10.1016/j.gca.2006.06.1563

Lee, M.J., Lee, J.I., 2017. Holocene eruptive history of Mt. Melbourne volcano, Antarctica: insights from tephra layers recorded from Talos Dome ice core. J. Geol. Soc. Korea, 53(4) 509-519. https://doi.org/10.14770/jgsk.2017.53.4.509

Lee, M.J., Kyle, P.R., Iverson, N.A., Lee, J.I., Han, Y., 2019. Rittmann volcano, Antarctica as the source of a widespread 1252 ± 2 CE tephra layer in Antarctica ice. Earth Planet. Sci. Lett. 521, 169–176. https://doi.org/10.1016/j.epsl.2019.06.002

Lee, M.J., Kim, G.B., Kyle, P.R., Lee, J.I., 2020a. Holocene eruption episodes of Mt. Melbourne, Antarctica: Constraints from proximal-distal tephra correlations. Goldschmidt 2020 Abstract https://doi.org/10.46427/gold2020.1439

Lee, J.I., Lee, M.J., Kim, G.B., Kyle, P.R., 2020b. Petrology of the most recent eruptions of Melbourne Volcano, Antarctica: insights into evolution of the magma plumbing system. Goldschmidt 2020 Abstract https://doi.org/10.46427/gold2020.1435

Lyon, G.L., 1986. Stable isotope stratigraphy of ice cores and the age of the last eruption at Mount Melbourne, Antarctica. New Zeal. J. Geol. Geophys. 29, 135–138. https://doi.org/10.1080/00288306.1986.10427528

McDonough, W.F., Sun, S.-s., 1995. The composition of the Earth. Chem. Geol. 120, 223–253. https://doi.org/https://doi.org/10.1016/0009-2541(94)00140-4

Min, K., Mundil, R., Renne, P.R., Ludwig, K.R., 2000. A test for systematic errors in 40Ar/39Ar geochronology through comparison with U/Pb analysis of a 1.1-Ga rhyolite. Geochim. Cosmochim. Acta 64, 73–98. https://doi.org/https://doi.org/10.1016/S0016-7037(99)00204-5

Narcisi, B., Petit, J.R., Chappellaz, J., 2010. A 70 ka record of explosive eruptions from the TALDICE ice core (Talos Dome, East Antarctic plateau). J. Quat. Sci. 25, 844–849. https://doi.org/https://doi.org/10.1002/jqs.1427

814 Narcisi, B., Petit, J.R., Delmonte, B., Scarchilli, C., Stenni, B., 2012. A 16,000-yr
815 tephra framework for the Antarctic ice sheet: a contribution from the new Talos Dome
816 core. Quat. Sci. Rev. 49, 52–63.
817 https://doi.org/https://doi.org/10.1016/j.quascirev.2012.06.011

818 Narcisi, B., Petit, J.R., 2021. Chapter 6.2 Englacial tephras of East Antarctica. Geol.
819 Soc. London, Mem. 55, 649 LP – 664. https://doi.org/10.1144/M55-2018-86

820 Nardin, R., Severi, M., Amore, A., Becagli, S., Burgay, F., Caiazzo, L., Ciardini, V.,
821 Dreossi, G., Frezzotti, M., Hong, S.-B., Khan, I., Narcisi, B.M., Proposito, M.,
822 Scarchilli, C., Selmo, E., Spolaor, A., Stenni, B., Traversi, R., 2021. Dating of an East
823 Antarctic ice core (GV7) by high resolution chemical stratigraphies. Clim. Past
824 Discuss. 2021, 1–27. https://doi.org/10.5194/cp-2021-44

825 Niespolo, E.M., Rutte, D., Deino, A.L., Renne, P.R., 2017. Intercalibration and age of
826 the Alder Creek sanidine $^{40}Ar/^{39}Ar$ standard. Quat. Geochronol. 39, 205–213.
827 https://doi.org/10.1016/j.quageo.2016.09.004

828 Rocchi, S., Smellie, J.L., 2021. Chapter 5.1b Northern Victoria Land: petrology. Geol.
829 Soc. London, Mem. 55, 383 LP – 413. https://doi.org/10.1144/M55-2019-19

830 Sims, K.W.W, Aster, R.C, Gaetani, G., Blichert-Toft, J., Phillips, E.H., Wallace, P.J.,
831 Mattioli, G.S., Rasmussen, D., Boyd, E.S.,, 2021. Chapter 7.2 Mount Erebus. Geol.
832 Soc. London, Mem. 55, 695-739. https://doi.org/10.1144/M55-2019-8

833 Severi, M., Udisti, R., Becagli, S., Stenni, B., Traversi, R., 2012. Volcanic
834 synchronisation of the EPICA-DC and TALDICE ice cores for the last 42 kyr BP.
835 Clim. Past 8, 509–517. https://doi.org/10.5194/cp-8-509-2012

836 Smellie, J.L., Rocchi, S. 2021. Chapter 5.1a Northern Victoria Land: volcanology. Soc.
837 London, Mem. 55(1), 347. http://dx.doi.org/10.1144/M55-2018-60

838 Sun, S.-s., McDonough, W.F., 1989. Chemical and isotopic systematics of oceanic
839 basalts: implications for mantle composition and processes. Geol. Soc. London, Spec.
840 Publ. 42, 313 LP – 345. https://doi.org/10.1144/GSL.SP.1989.042.01.19

841 Tomlinson, E.L., Thordarson, T., Müller, W., Thirlwall, M., Menzies, M.A., 2010.
842 Microanalysis of tephra by LA-ICP-MS - Strategies, advantages and limitations
843 assessed using the Thorsmörk ignimbrite (Southern Iceland). Chem. Geol. 279, 73–89.
844 https://doi.org/10.1016/j.chemgeo.2010.09.013

845 Walker, G.P.L. 1985. Origin of coarse lithic breccias near ignimbrite source vents. J.
846 Volcanol. Geotherm. Res. 25(1–2), 157-171. https://doi.org/10.1016/0377-
847 0273(85)90010-1.

848 White, J.D.L., Houghton, B.F., 2006. Primary volcaniclastic rocks. Geology, 34, 677–
849 680. https://doi.org/10.1130/G22346.1

850 Wilson, L., Sparks, R.S.J., Walker, G.P.L., 1980. Explosive volcanic eruptions — IV.
851 The control of magma properties and conduit geometry on eruption column behaviour.
852 Geophys. J. Int. 63, 117–148. https://doi.org/10.1111/j.1365-246X.1980.tb02613.x

853 Wörner, G., Viereck, L., 1990. Individual Volcano Descriptions A10: Mt. Melbourne.
854 Antarct. Res. Ser., 48, 72-78.

855 Wörner, G., Viereck, L., Hertogen, J., Niephaus, H., 1989. The Mt. Melbourne
856 Volcanic Field (Victoria Land, Antarctica) II: Geochemistry and magma genesis.
857 Geologisches Jahrbuch E, 38, 395-433

858 Yang, J.-W., Han, Y., Orsi, A.J., Kim, S.-J., Han, H., Ryu, Y., Jang, Y., Moon, J., Choi,
859 T., Hur, S. Do, Ahn, J., 2018. Surface Temperature in Twentieth Century at the Styx
860 Glacier, Northern Victoria Land, Antarctica, From Borehole Thermometry. Geophys.
861 Res. Lett. 45, 9834–9842. https://doi.org/https://doi.org/10.1029/2018GL078770

862

863 **Captions**

Figure 1. (A) Map of Antarctica showing the locations of Mount Melbourne volcano and Antarctic deep and shallow ice cores and blue ice field (circles). (B) Map of Mount Melbourne and locations of the studied stratigraphic sections (S1-S5).

Figure 2. A) Picture of Mount Melbourne taken from Mario Zucchelli Station located about 40 km south of the volcano; B) the bottom of the summit crater filled by snow and the rim is observed on the left of the picture. In the background, two scoria cones are visible.

Figure 3. Pictures and schematic logs of the stratigraphic sections S1, S2 and S4.

Figure 4. Pictures of: A) northern summit area covered by black bombs that range from around a meter to centimeters in size (sample MELS1-5); B) a parasitic scoria cone in the northern flank of Mount Melbourne; C) trachytic pumice deposit exposed at the top of the parasitic scoria cone in B (section S3); D) small outcrop of the scoria deposit covered by snow, which is located in the southern side of the summit crater (section S5; sample MELS5-1).

Figure 5. SEM backscatter images of studied products showing textural features of Mount Melbourne volcanic products. A) Sample MELS1-1 is a porphyritic scoria from the lowermost lapilli deposit; it consists of phenocrysts of plagioclase in a glassy groundmass rich of skeletal microlites; B) Sample MELS1-3 represents a pumice of the main pyroclastic fallout unit; it has highly vesicular and glassy groundmass with phenocrysts of feldspars showing sieve texture; C) Sample MELS1-5 represents scoriaceous bombs scattered over the pumice deposit; it is a low porphyritic scoria with phenocrysts dispersed in a groundmass with abundant acicular microlites of feldspar; D) Sample MELS5-1 represents the scoriaceous bombs and lapilli overlaying the pumice deposits; it is a high porphyritic scoria with abundant phenocrysts in a glassy groundmass.

Figure 6. Major element glass geochemical variation of Mount Melbourne tephra compared with volcanic glasses of explosive eruption deposits produced by Mount

Rittmann (Di Roberto et al., 2019; Lee et al., 2019), The Pleiades (Lee et al., 2019), Mount Melbourne (Lee et al., 2019), and Erebus volcano (Harpel et al., 2008). A-b) Total alkali-silica diagram (TAS; LeBas et al., 1986), C) K_2O vs SiO_2 diagram, and D) CaO vs SiO_2 diagrams showing the glass composition of studied products from Mount Melbourne. Error bars represented 2 standard deviations of replicated analyses of the MPI-DING StHs6/80-G secondary standard glass run alongside the marine tephra samples

Figure 7. Selected trace element compositions of studied samples and comparison with bulk rock compositions from literature: MB-07 and MB-43 from Armienti et al. (1991); SE 03 157, SE 04 158, MM 05-185, MM 05-229, MM 15-229 from Worner et al. (1989).

Figure 8. Primitive mantle (PM) normalized spider diagram (McDonough and Sun, 1995) showing the trace element distribution of the studied samples.

Figure 9. Age and K/Ca (derived from neutron-produced $^{39}Ar_K/^{37}Ar_{Ca}$ ratio) profiles from step-heating experiments of two aliquots of feldspar separate from sample MELS1-3. Data were acquired by a single-collector noble gas mass spectrometer (MAP215-50, orange spectra) and a multi-collector noble gas mass spectrometer (ARGUS VI, green spectra). Box heights indicate the 2σ analytical uncertainty.

Figure 10. Map of the summit area of Mount Melbourne volcano modified after that published by Worner and Viereck (1990), and integrated by field observations and analysis of satellite images. The distribution of deposits of the studied eruptions is reported along with the precise position of stratigraphic sections

Supplemental Table 1. Major-element and trace-element data of single glass shards.

Supplemental Table 2. Full ^{40}Ar-^{39}Ar laser data on feldspar MELS1-3.

916 Supplemental Table 3. Composition of feldspar from MELS1-1 and MELS1-3
917 samples.

Figure 1

Click here to access/download;Figure;Figure 1.jpg

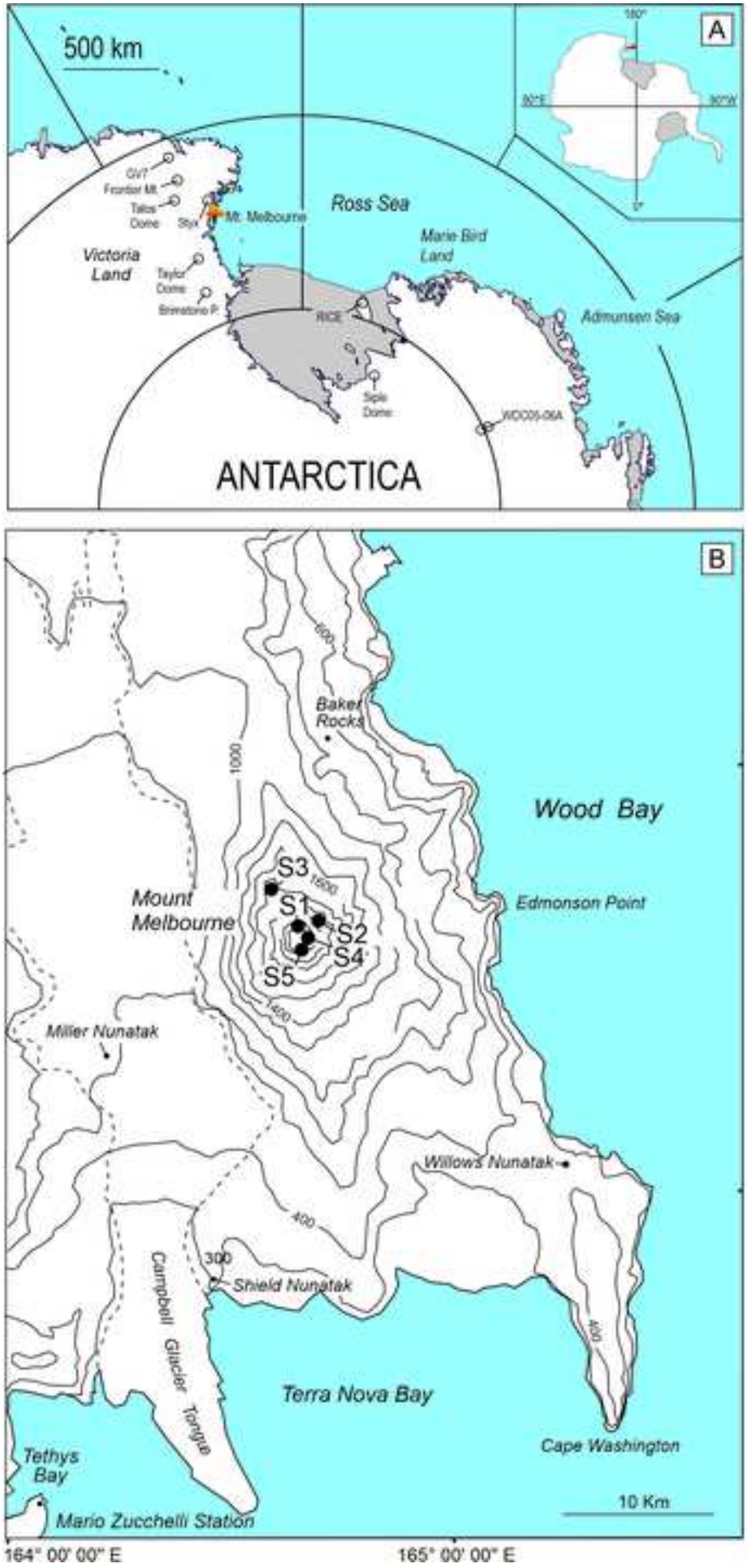

Figure 2

Click here to access/download;Figure;Figure 2.jpg

Figure 3

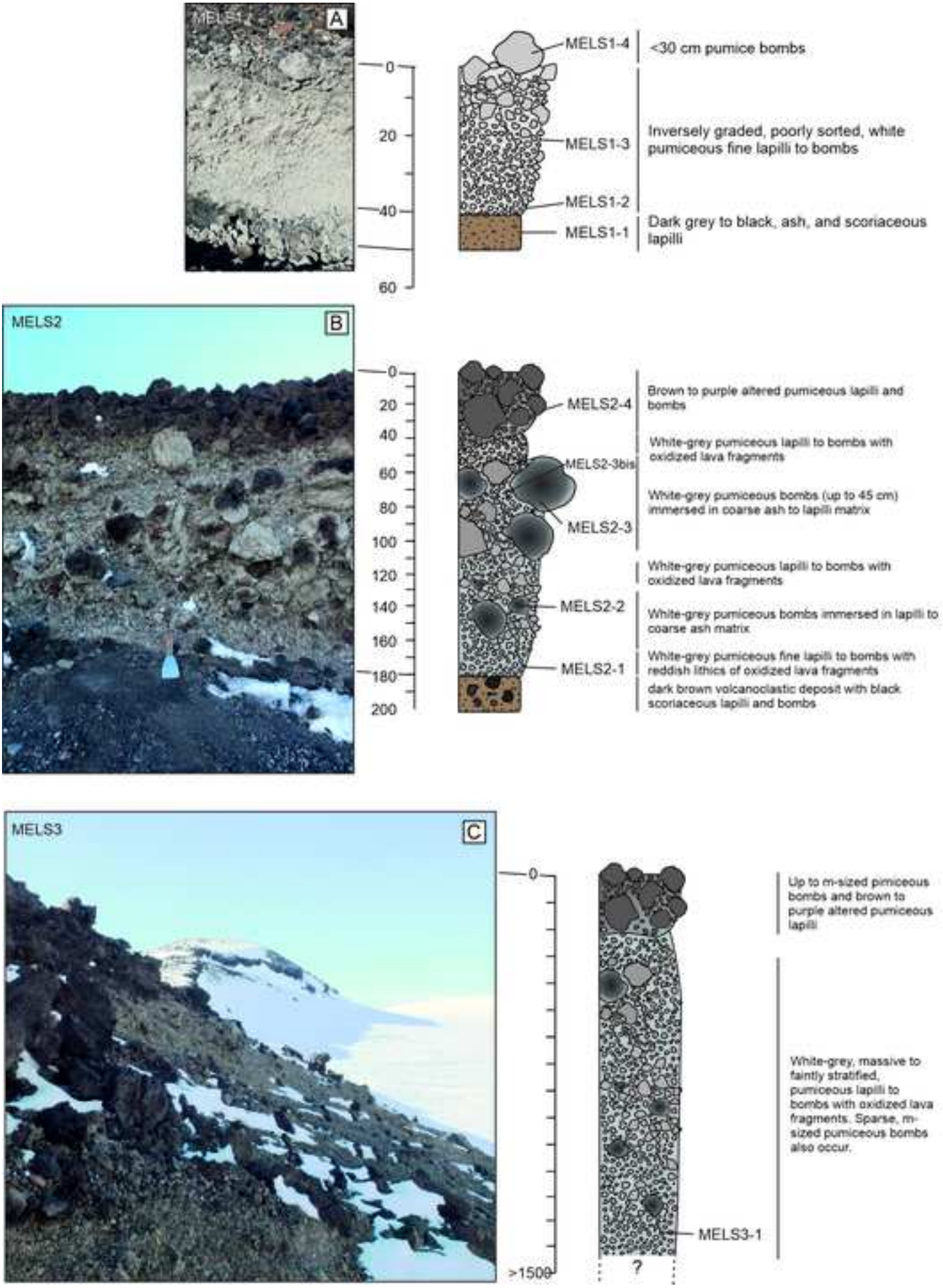

Figure 4

Click here to access/download;Figure;Figure 4.jpg

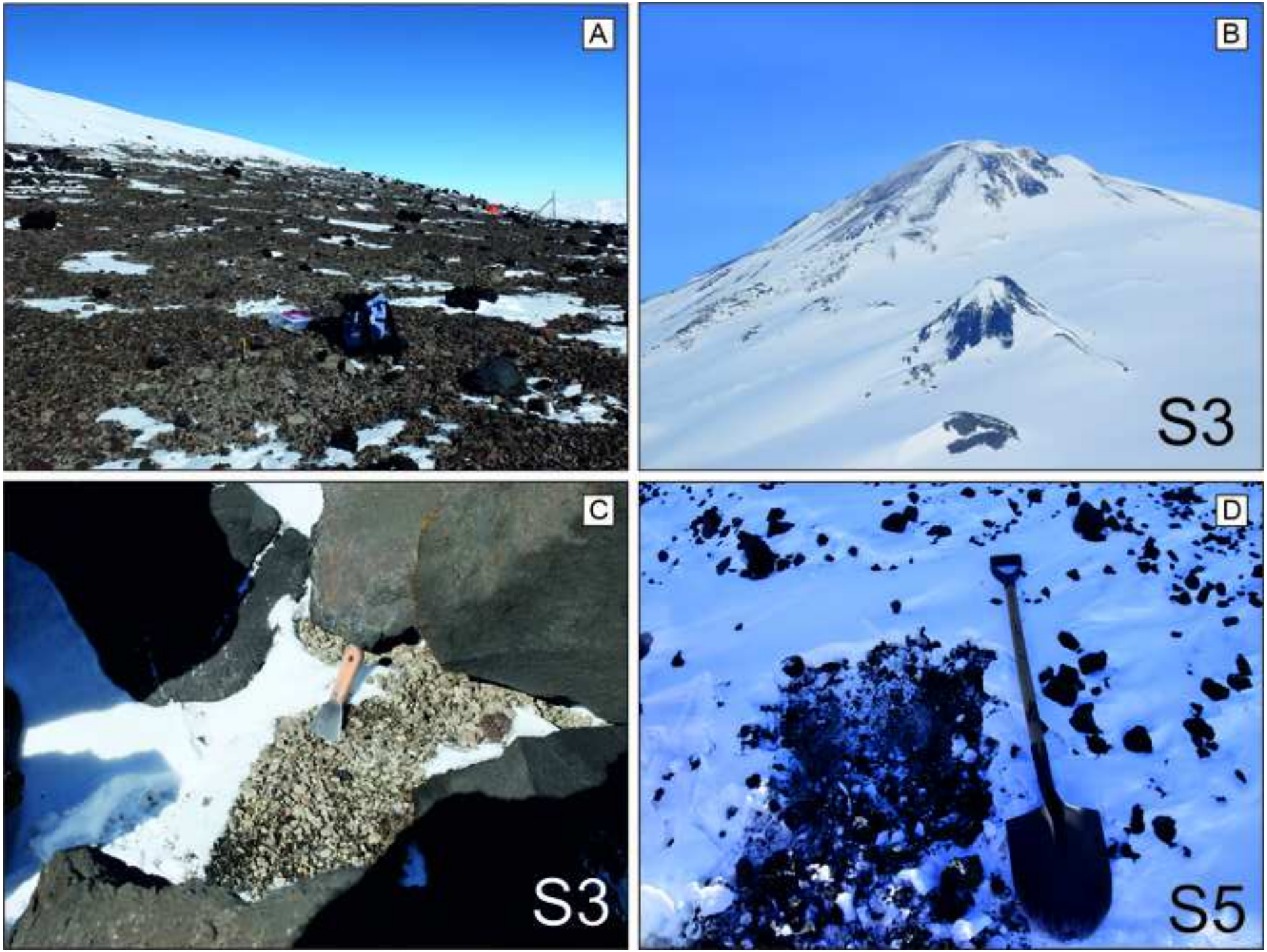

Figure 5

Click here to access/download;Figure;Figure 5.tif

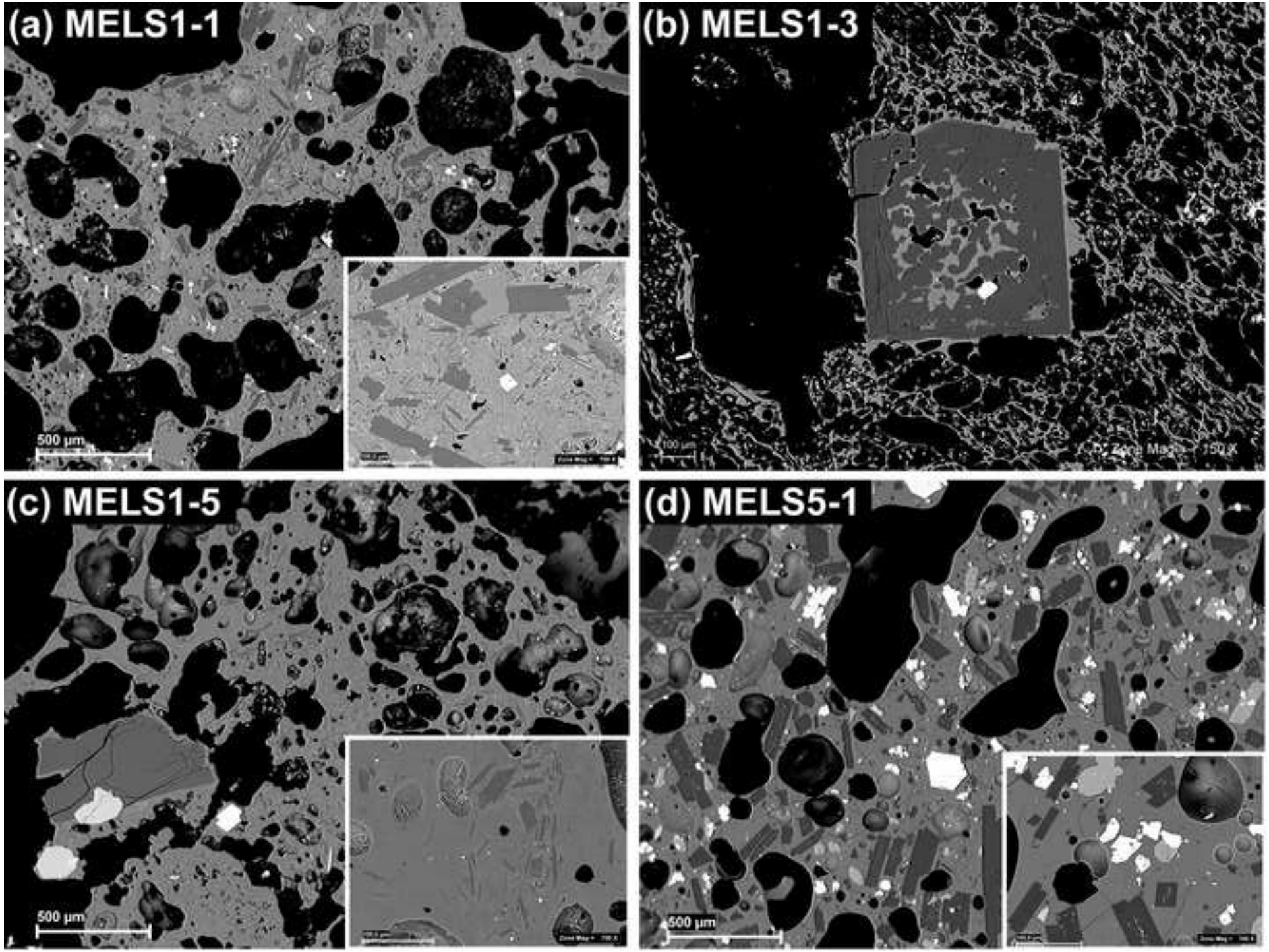

Figure 6

Click here to access/download;Figure;Figure 6.jpg

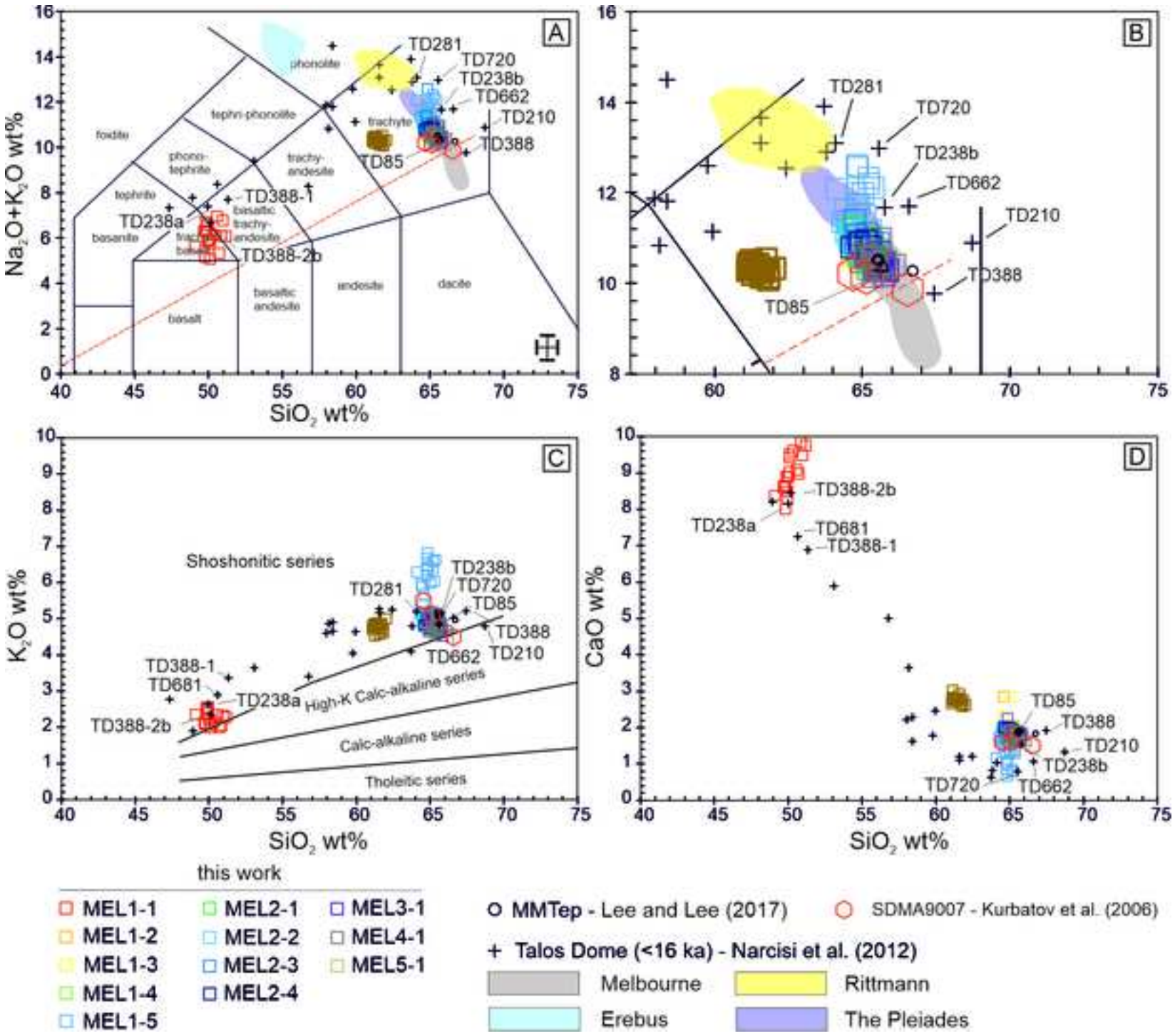

Figure 7

Click here to access/download;Figure;Figure 7.jpg

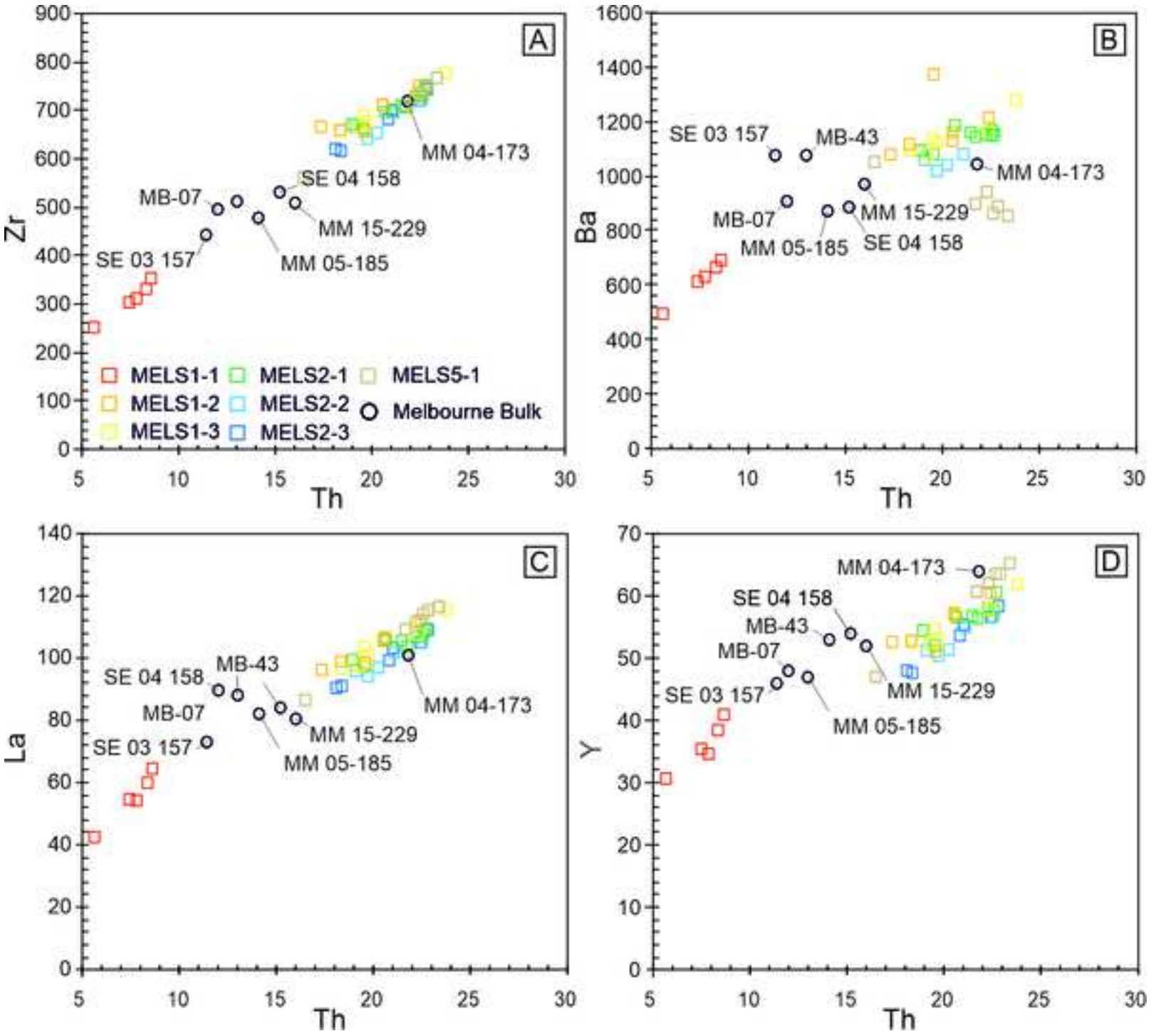

Figure 8

Click here to access/download;Figure;Figure 8.jpg

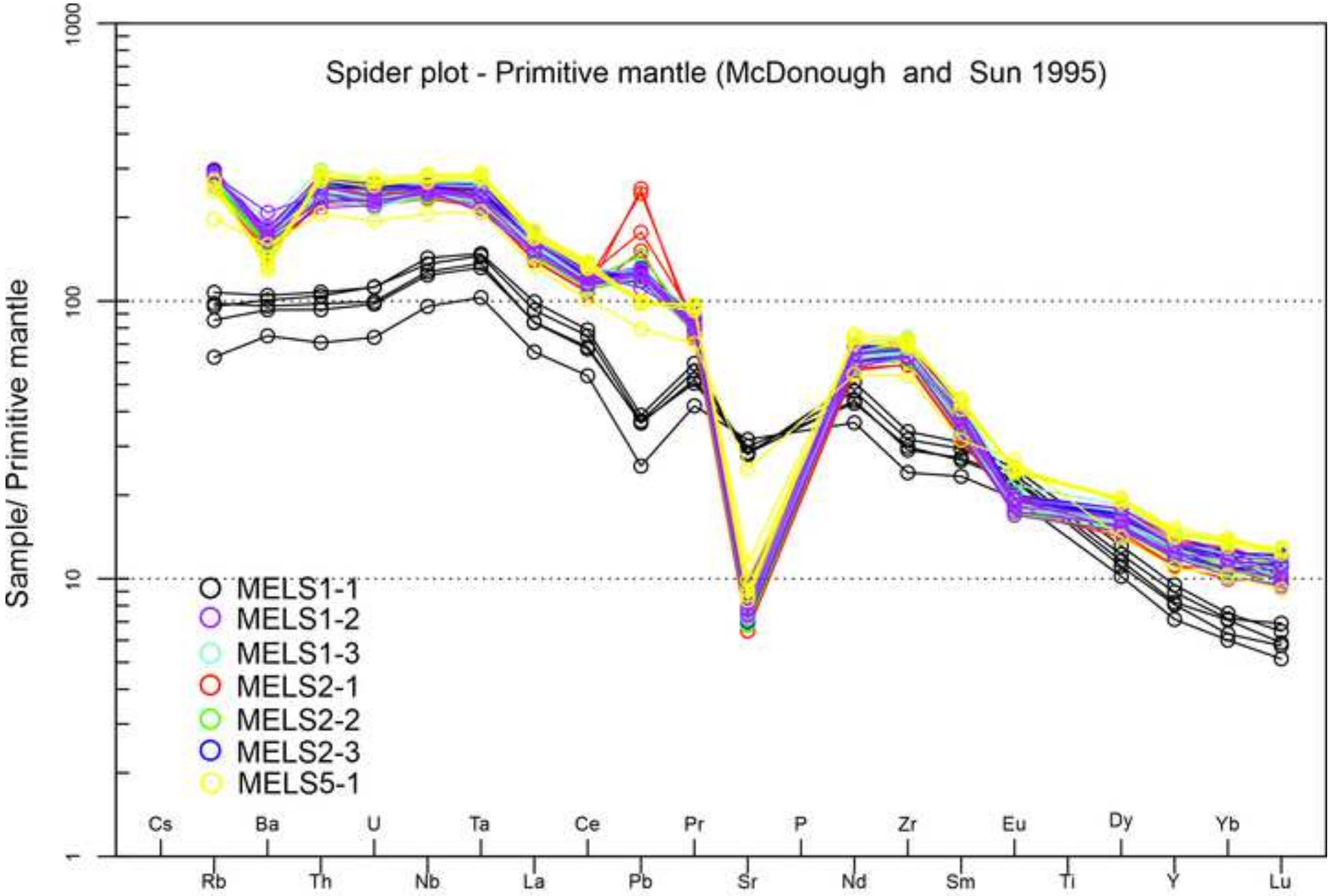

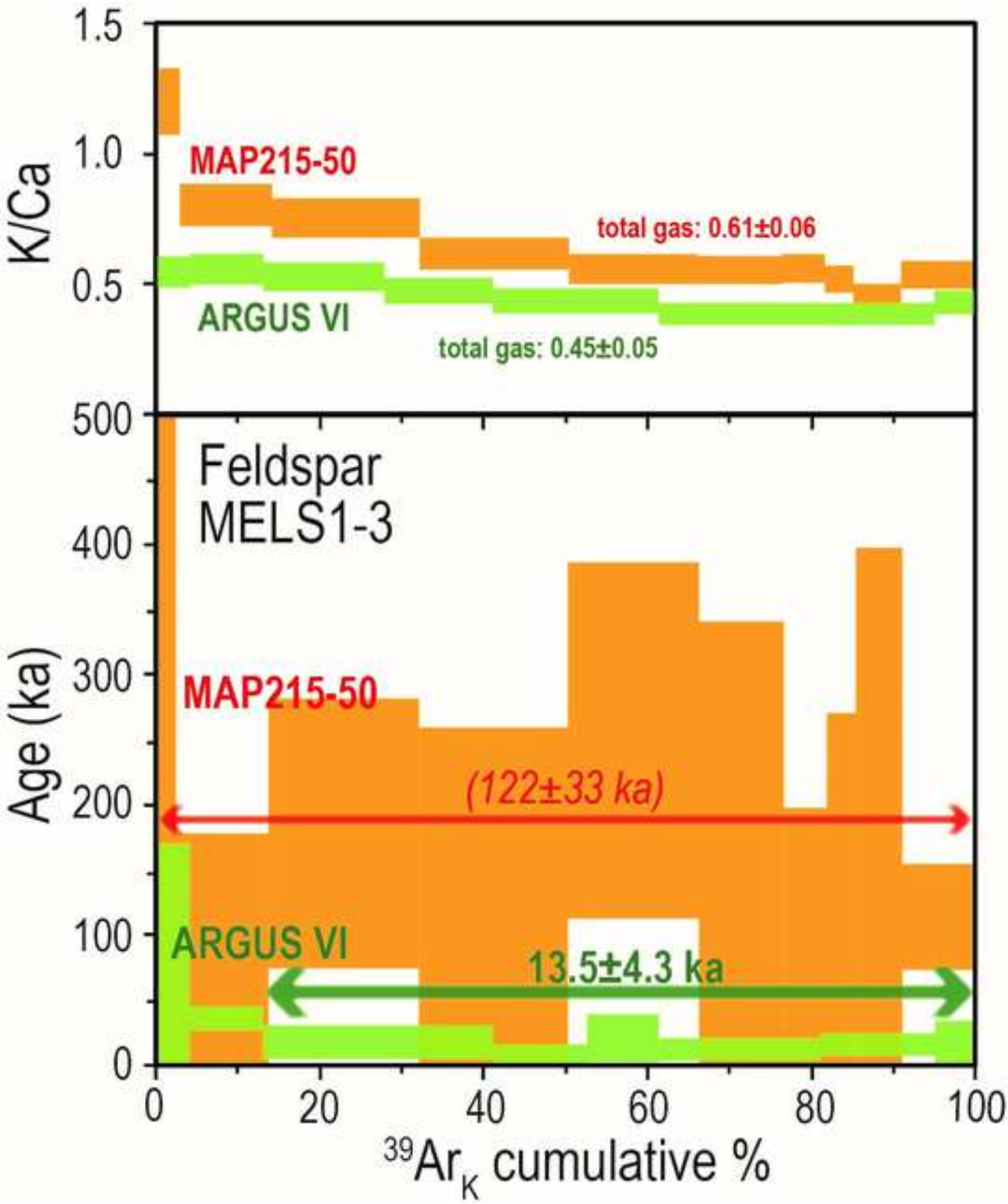

Figure 10

Click here to access/download;Figure;Fig. 10.jpg

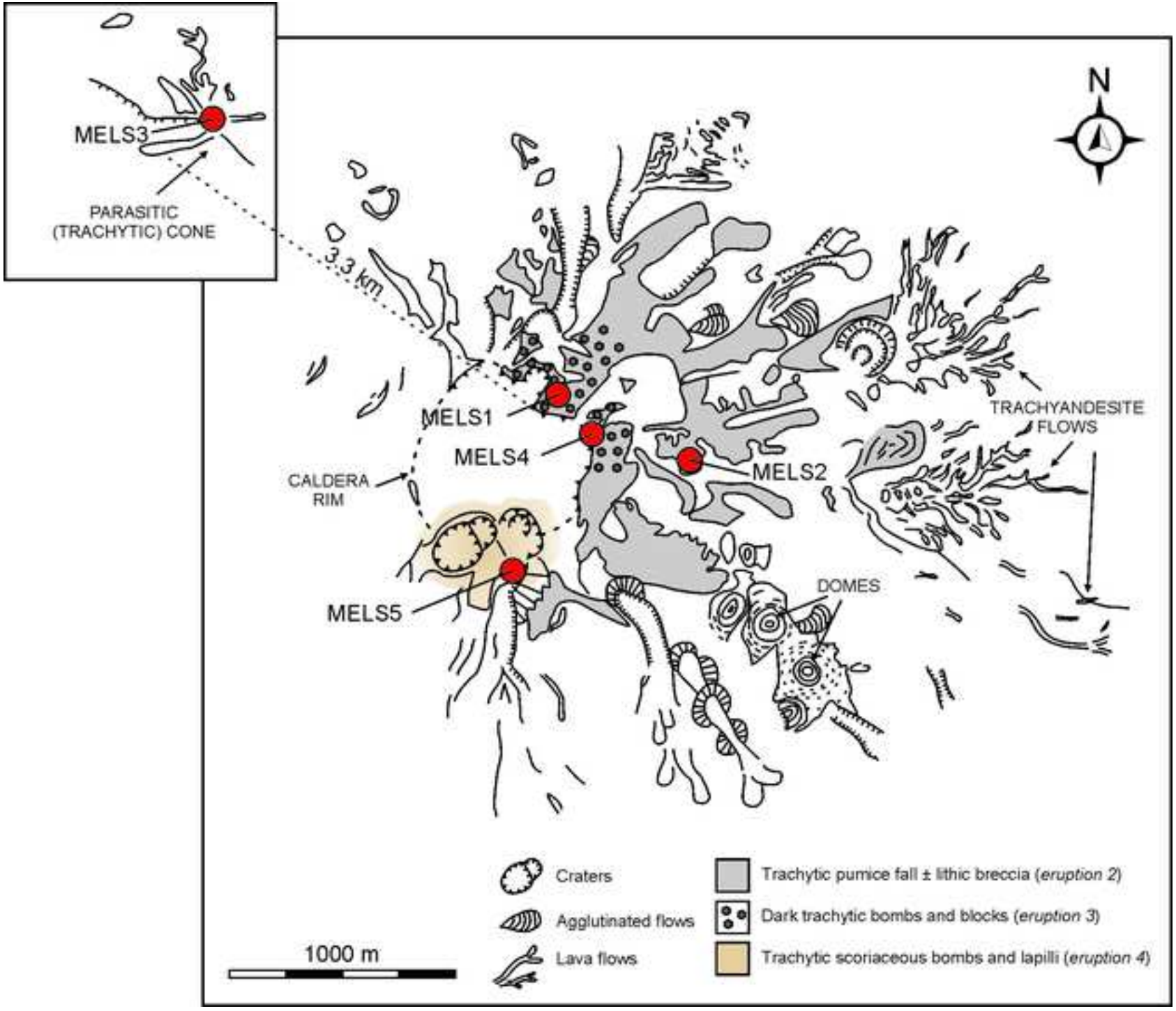

Credit Author Statement

P.D.C. and A.C. carried out the fieldwork and sampling on the flanks of Mount Melbourne. P.D.C. and A.D.R. and conceived the research and with the help of G.R. carried out the textural analyzes of the volcanic glass, the petrographic analyzes and interpreted geochemical and petrological data. P.A, M.N and V.S carried out the major- and trace-element geochemical analyses, respectively. G.D.V performed the ^{40}Ar-^{39}Ar analyses and data interpretation. All authors contributed to data interpretation, the writing of the manuscript and the preparation of the figures.